



HAL
open science

Ganymede's atmosphere as constrained by HST/STIS observations

François Leblanc, L. Roth, Jean-Yves Chaufray, Ronan Modolo, M. Galand, Nickolay Ivchenko, Gianluca Carnielli, Claire Baskevitch, A. Oza, Elisabeth Werner

► **To cite this version:**

François Leblanc, L. Roth, Jean-Yves Chaufray, Ronan Modolo, M. Galand, et al.. Ganymede's atmosphere as constrained by HST/STIS observations. *Icarus*, 2023, 399, pp.115557. 10.1016/j.icarus.2023.115557 . insu-04056918

HAL Id: insu-04056918

<https://insu.hal.science/insu-04056918>

Submitted on 5 Jul 2023

HAL is a multi-disciplinary open access archive for the deposit and dissemination of scientific research documents, whether they are published or not. The documents may come from teaching and research institutions in France or abroad, or from public or private research centers.

L'archive ouverte pluridisciplinaire **HAL**, est destinée au dépôt et à la diffusion de documents scientifiques de niveau recherche, publiés ou non, émanant des établissements d'enseignement et de recherche français ou étrangers, des laboratoires publics ou privés.

1 **Ganymede's atmosphere as constrained by HST/STIS observations**

2

3 F. Leblanc¹, Roth L.², Chaufray J.Y.¹, R. Modolo¹, M. Galand³, N. Ivchenko², G.

4 Carnielli³, C. Baskevitch¹, A. Oza⁴ and A.L.E. Werner^{1,5}

5

6 ¹ LATMOS/CNRS, Sorbonne Université, UVSQ, Paris, France

7 ² Space and Plasma Physics, KTH Royal Institute of Technology, Stockholm, Sweden

8 ³ Department of Physics, Imperial College London, London, UK

9 ⁴ Jet Propulsion Laboratory, California Institute of Technology, Pasadena, USA

10 ⁵ Now at Swedish Institute of Space Physics, Uppsala, Sweden

11

12

13 **Abstract**

14 A new analysis of aurora observations of Ganymede's atmosphere on the orbital leading and trailing
15 hemispheres has been recently published by Roth et al. (2021), suggesting that water is its main
16 constituent near noon. Here, we present two additional aurora observations of Ganymede's sub-Jovian
17 and anti-Jovian hemispheres, which suggest a modulation of the atmospheric H₂O/O₂ ratio on the
18 moon's orbital period, and analyze the orbital evolution of the atmosphere. For this, we propose a
19 reconstruction of aurora observations based on a physical modelling of the exosphere taking into
20 account its orbital variability (the Exospheric Global Model; Leblanc et al. 2017). The solution described
21 in this paper agrees with Roth et al. (2021) that Ganymede's exosphere should be dominantly
22 composed of water molecules. From Ganymede's position when its leading hemisphere is illuminated
23 to when it is its trailing hemisphere, the column density of O₂ may vary between 4.3×10^{14} and 3.6×10^{14}
24 cm⁻² whereas the H₂O column density should vary between 5.6×10^{14} and 1.3×10^{15} cm⁻². The water
25 content of Ganymede's atmosphere is essentially constrained by its sublimation rate whereas the O₂
26 component of Ganymede's atmosphere is controlled by the radiolytic yield. The other species,
27 products of the water molecules, vary in a more complex way depending on their sources, either as
28 ejecta from the surface and/or as product of the dissociation of the other atmospheric constituents.
29 Electron impact on H₂O and H₂ molecules is shown to likely produce H Lyman-alpha emissions close to
30 Ganymede, in addition to the observed extended Lyman-alpha corona from H resonant scattering. All
31 these conclusions being highly dependent on our capability to accurately model the origins of the
32 observed Ganymede auroral emissions, modelling these emissions remains poorly constrained without
33 an accurate knowledge of the Jovian magnetospheric and Ganymede ionospheric electron
34 populations.

35 I Introduction

36 As summarized in Roth et al. (2022), only very few direct observations of Ganymede's atmosphere
37 have been realized so far. The very first evidence of Ganymede's atmosphere was obtained by Galileo
38 FUV instrument in 1996 (Barth et al. 1997) and revealed an extended atmosphere of H atoms, an
39 observation later confirmed by the Space Telescope Imaging Spectrograph of the Hubble Space
40 Telescope (HST/STIS; Feldman et al. 2000; Alday et al. 2017). Alday et al. (2017) concluded that the
41 Lyman α emission brightness does not vary along Ganymede's orbit with an average corona emission
42 intensity of ~ 320 R corresponding to a column density of $1.55 \pm 1.2 \times 10^{12}$ H/cm² if only produced by
43 resonant scattering. Recent HST/STIS observations of Ganymede in transit (Roth et al. 2023) found
44 weak but widely extended absorption around the moon, confirming the H corona profile and densities
45 derived earlier. In 1996, the Goddard High Resolution Spectrograph of the Hubble Space Telescope
46 (HST/GHRS) obtained the first evidence of two other emission lines at 130.4 and 135.6 nm from
47 Ganymede's atmosphere (Hall et al. 1998). The ratio of these two emissions strongly suggested that
48 these observed emissions were probably due to electron impact on O₂ molecules. Moreover, the first
49 images of these emission lines obtained by HST/STIS clearly showed that the 135.6 nm was confined
50 in the polar regions (Hall et al. 1998) and even roughly collocated to the open-closed field line boundary
51 (OCFB) of Ganymede magnetosphere (McGrath et al. 2013; Molyneux et al. 2018). The auroral nature
52 of these two emissions implies that their brightnesses depend essentially on three parameters: the
53 column density and composition of the neutral atmosphere and the energy flux distribution of the
54 electrons. When supposing that the observed emission was only produced by electron impact on O₂,
55 without a knowledge of the electron distribution in these regions, the column density of O₂/cm² could
56 not be estimated very accurately and was inferred to be between 10^{14} to 10^{15} O₂/cm² (Hall et al. 1998;
57 Molyneux et al. 2018). No observation constraining the H₂O, OH and H₂ exosphere of Ganymede has
58 been obtained up to Roth et al. (2021), whereas the oxygen atomic species was tentatively identified
59 (Molyneux et al. 1998; Roth et al. 2021).

60

61 Considering the relatively limited number of observations and the difficulty to realize new ones,
62 modelling Ganymede's atmosphere remains presently our best approach to get an idea on how this
63 atmosphere might be spatially organized and temporarily variable. This atmosphere is thought to be
64 essentially composed of H₂O, O₂ and their products. H₂O is essentially produced by sublimation near
65 the subsolar point, which according to Marconi (2007), Shematovitch (2016) and Leblanc et al. (2017)
66 leads to a partially surface bounded exosphere in reference to the Moon exosphere (Stern 1999). But
67 H₂O can also be produced by the sputtering of Ganymede icy surface (Cassidy et al. 2013) at high
68 latitudes.

69 Our ability to model Ganymede's atmosphere depends therefore on several parameters:

70 - the surface temperature and composition (Spencer et al. 1989; Leblanc et al. 2017),

71 - the spatial dependency of the ion bombardment of the surface by the Jovian particles (Plainaki et al.
72 2020a, b; Vorburger et al. 2022) but also by ions produced locally in Ganymede's neutral atmosphere
73 (Carnielli et al. 2020b),

74 - the ejection rate induced by the sputtering (Cooper et al. 2001; Turc et al. 2014; Plainaki et al. 2015;
75 2020a, b and Carnielli et al. 2020a, b) and by sublimation (Johnson et al. 1989; Fray and Schmitt 2009;
76 Leblanc et al. 2017; Vorburger et al. 2022),

77 - the losses by photon and electron ionization and dissociation, as well as by reabsorption at the surface
78 and by neutral and ion escape,

79 - the orbital variability of all these parameters (Plainaki et al. 2015; Leblanc et al. 2017).

80 Recently, Roth et al. (2021) proposed an original analysis of new and old HST/STIS observations
81 obtained at two different orbital positions of Ganymede. These authors suggested that the radial
82 distribution of the 130.4 nm and 135.6 nm emission lines brightness was consistent with the existence
83 of a dominant H₂O atmospheric component and with its predicted orbital variability. Based on a simple
84 symmetric model of the atmosphere, Roth et al. (2021) concluded that Ganymede's atmosphere water

85 column density peaks at a value of 6×10^{15} H₂O/cm² near the center of the visible disk when the trailing
86 hemisphere is illuminated, a value which decreases to 1×10^{15} H₂O/cm² when the leading hemisphere
87 of Ganymede is illuminated.

88 In the following, we present a detailed comparison between these observations and the results of
89 simulation performed with Exospheric Global Model, EGM (Leblanc et al. 2017; Oza et al. 2019). In
90 section II, we briefly describe the set of observations analyzed in this paper, in section III, our model,
91 whereas in section IV a detailed comparison and discussion of the main lessons from such a comparison
92 are provided. Section V summarizes the main conclusions of this work.

93

94 **II HST/STIS Observations**

95 Roth et al. (2021) reported the first indirect observation of Ganymede water atmosphere. They used
96 two sets of images by Hubble's Space Telescope Imaging Spectrograph (HST/STIS) performed at two
97 positions of Ganymede along its orbit:

98 - at a phase angle of $98^\circ - 111^\circ$ (2010-11-19, Figure 1 in yellow), that is with the leading hemispheric
99 side of Ganymede being illuminated,

100 - at a phase angle of $289^\circ - 300^\circ$ (1998-10-30, Figure 1 in blue), that is with the trailing hemispheric
101 side of Ganymede being illuminated.

102 In addition, Roth et al. (2021) analyzed spectra taken with HST's Cosmics Origins Spectrograph (COS)
103 at a phase angle of $352^\circ - 357^\circ$, that is just before and partly when Ganymede is in the shadow of
104 Jupiter. At such phase angle, they reported no significant change in the relative intensity of the two
105 oxygen lines, 130.4 and 135.6 nm, suggesting that the atomic oxygen atmospheric content should
106 not exceed 2×10^{12} O/cm². In the following, we will not use the COS spectra in our analysis because
107 these observations were only used to estimate an upper limit for the exospheric content in atomic
108 oxygen and do not provide useful spatial information on the emissions.

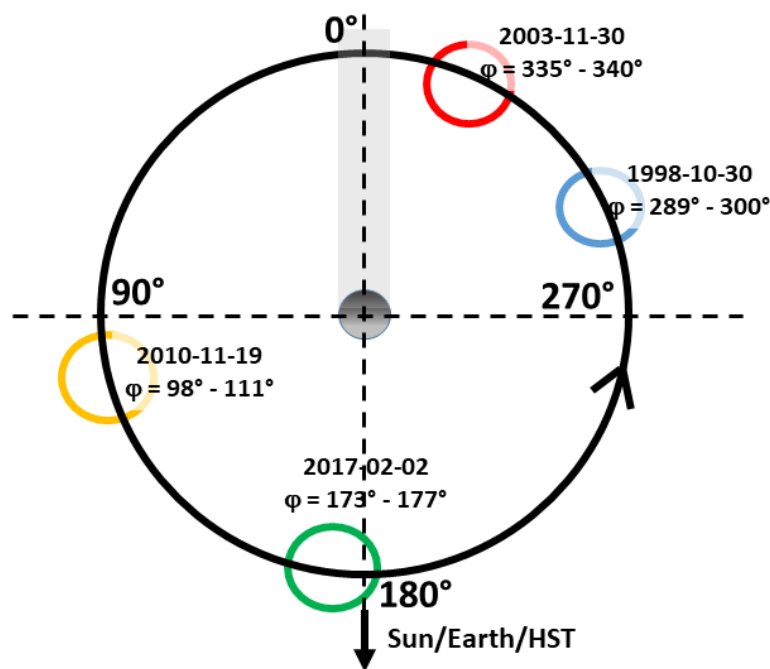
109 To the two sets of HST/STIS observations, we add two other sets of HST/STIS observations obtained
110 at two complementary positions of Ganymede (Figure 1; Marzok et al. 2022):

- 111 - at a phase angle of $173\text{-}177^\circ$ obtained with STIS on the 02/02/2017 (Figure 1, in green),
- 112 - at a phase angle of $335^\circ\text{-}340^\circ$ obtained with STIS on the 11/30/2003 (Figure 1, in red).

113 These two later sets of observations nicely complete the ones described in Roth et al. (2021) even if
114 obtained with lower signal/noise ratio (Figure 2) and allow us to track the atmospheric orbital
115 variability. The 135.6 nm images have been published in McGrath et al. (2013) (2003 dataset) and
116 Marzok et al. (2022) (2017 dataset). For this study, the 130.4 images obtained simultaneously were
117 analyzed for the first time and are used in addition. The data processing and image analysis of the
118 new datasets follows the same steps as described in Roth et al. (2021), Roth et al. (2016) and (2014):

- 119 - Earth 130.4 nm Geocorona is taken into account by selecting low-Geocorona exposures when HST
120 was in Earth's nightside and by monitoring the 130.4 nm background signal as HST moves into Earth's
121 shadow (Roth et al. 2016). The background induced by the Geocorona, interplanetary medium and
122 torus emissions is also estimated and subtracted using two regions far from Ganymede disk along the
123 slit (Roth et al. 2014).
- 124 - Solar reflected light from Ganymede's surface (surface albedo) is subtracted from the observation
125 using UV daily observations by SORCE/SOLSTICE instrument (McClintock et al. 2005) taking into
126 account STIS G140L resolution and using a homogeneous bright model disk of Ganymede convolved
127 with STIS Point Spread Function and adjusted to match the observed surface reflection signal
128 between 143 and 153 nm. We have tested different phase angle dependencies for the surface
129 reflection between a uniform disk (as used in Roth et al. 2021) and a Lambertian reflector using the
130 description from Oren and Nayar (1994). The effects on the resulting emission ratio is less than 10%
131 and for the presented results we used the simple uniform disk reflectance.

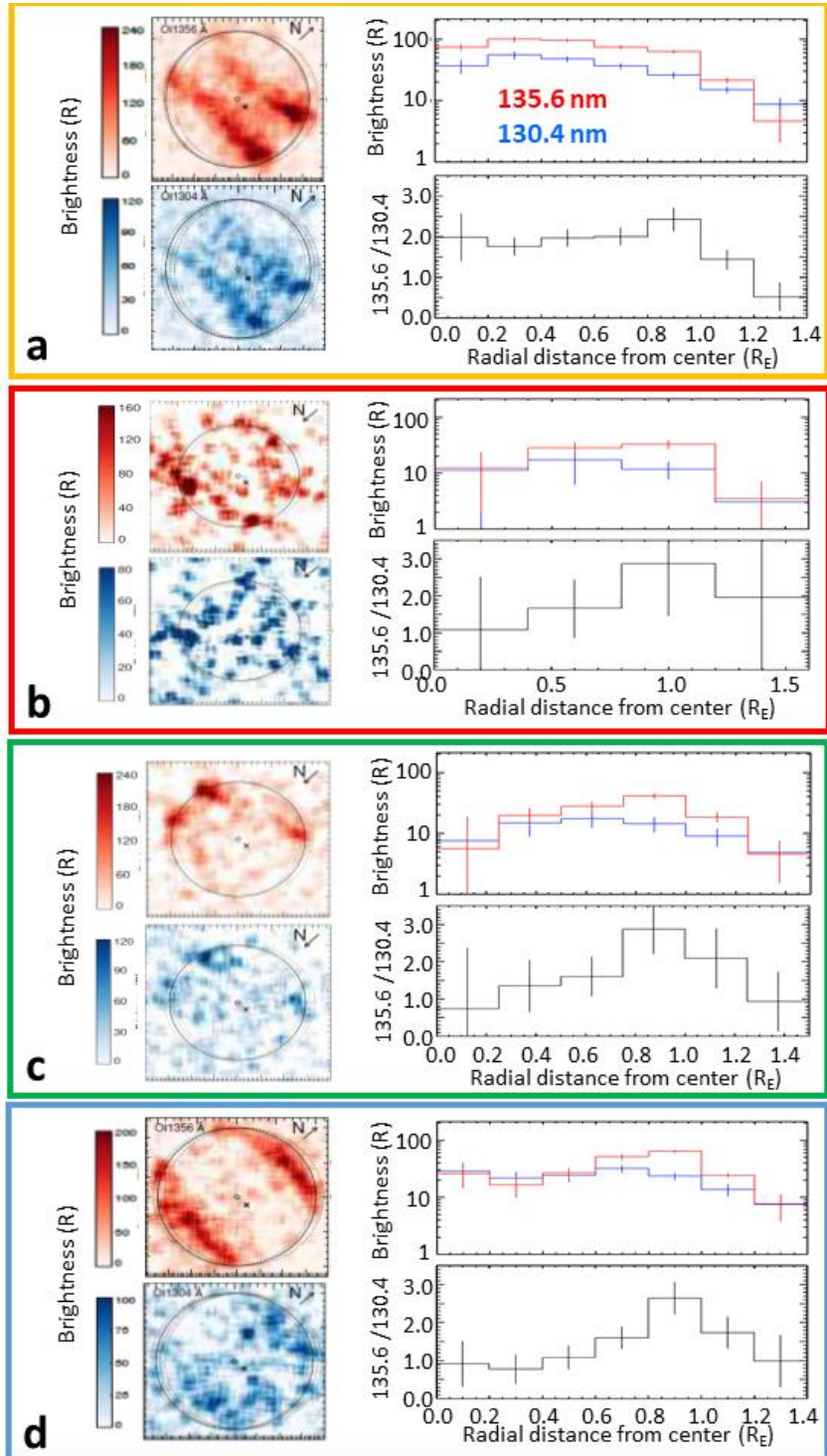
132 From the corrected HST/STIS images, we calculated the radial profiles of the intensity of the 130.4
 133 and 135.6 nm emissions by integrating its brightness on annulus centred on Ganymede's disk and
 134 binned in steps of $0.2 R_G$ for the observations obtained at a phase angle of 98° - 111° and 298° - 300°
 135 (panels a and d in Figure 2), of $0.4 R_G$ for a phase angle of 335° - 340° (panel b in Figure 2) and of 0.25
 136 R_G for a phase angle of 173° - 177° (panel c in Figure 2). The large bin size in panel b is chosen to get
 137 somewhat lower error bars while still keeping a reasonable number of 4 bins to actually see a radial
 138 profile trend.



139
 140 **Figure 1:** Positions of Ganymede during the four sets of observations of HST/STIS used in this paper. We
 141 also indicated the range of phase angle of each set of observations as well as their date. The caption
 142 colors of the circle refer to Figures 2 and 6.

143
 144 Figure 2 provides a view of the four sets of observations used in this paper. At the four orbital positions
 145 of Ganymede (Figure 1), HST/STIS realized 2D images of the emission brightness intensity of the 130.4
 146 nm and 135.6 nm emission lines (left panels of each set of observations) from which it was possible to

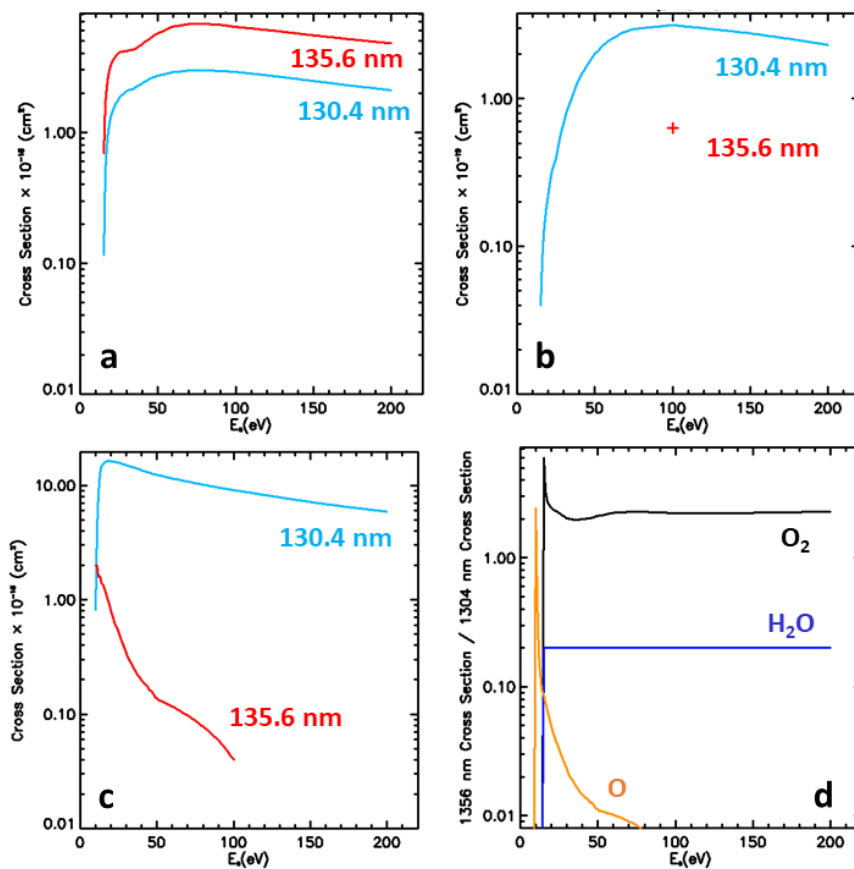
147 extract an average emission intensity profile with respect to the distance from the center of Ganymede
148 apparent disk (right top panel). We also derived the ratio of these two emissions lines as a function of
149 the distance from the center (right bottom panels). This ratio is displayed up to $1.4 R_G$ whereas the 2D
150 images show pixels up to at least $1.2 R_G$ (panel d). The observations use a long slit and the images
151 therefore do not go beyond the left and right edges shown in Figure 2, but above and below the
152 displayed images. However, because the signal-to-noise ratio of a single pixel is well below 1 at
153 distances $> 1.2 R_G$, we choose not to show those pixels above $1.2 R_G$ in these 2D images. When the
154 signal was low, we rather choose to integrate over few pixels to show a significant signal, not
155 necessarily showing the noisy spatially resolved data. As explained in Roth et al. (2021) and displayed
156 in Figure 3d, this ratio should be of ~ 2.3 if both emissions are produced by the electron impact on O_2
157 only. The ratio is close to ~ 0.2 if produced by electron impact on H_2O and is lower than 0.1 if produced
158 by electron impact on atomic O (Figure 3d).



159

160 **Figure 2:** Observation of Ganymede's atmospheric emission by HST/STIS. Each panel corresponds to
 161 one position displayed in Figure 1: a 2010-11-19, phase angle of 98° - 111° (Roth et al. 2021). b: 2003-
 162 11-30, phase angle of 335° - 340° (McGrath et al. 2013). c: 2017-02-02, phase angle of 173° - 177° . d:
 163 1998-10-30, phase angle between 289° - 300° (Roth et al. 2021). Each panel surrounded by a rectangle
 164 whose colour corresponds to that used for the circles in Figure 1 is composed of the STIS images of the

165 135.6 nm (red) and 130.4 nm (blue) brightness intensities, of the radial profile from the center of the
 166 disk up to around half a radius above the limb of the emission brightness intensity at these two
 167 wavelengths (top right panel in each rectangle where the red solid line corresponds to the 135.6 nm
 168 emission brightness and the blue solid line to the 130.4 nm emission brightness) and of the ratio of the
 169 135.6 nm emission intensity divided by the 130.4 nm emission intensity (bottom right panel in each
 170 rectangle). The North direction in panels b and c (pointing towards the bottom of the figure) is inverted
 171 with respect to the North direction in panels a and b (pointing towards the top of the figure).



172

173 **Figure 3:** Emission excitation electron impact cross sections. a: $O_2 + e$ (Kanik et al. 2003). b: $H_2O + e$
 174 (Makarov et al. 2004) and only available measurement of the $H_2O + e$ 135.6 nm at 100 eV (Roth et al.
 175 2021). c: $O + e$ (Tayal et al. 2016 for 135.6 nm; Johnson et al. 2005 for 130.4 nm). d: ratio of the 135.6
 176 nm / 130.4 nm emission excitation cross section for $O_2 + e$ (black line), $H_2O + e$ (blue line, with the
 177 assumption that the only measurement at 100 eV is valid on the whole range of electron energy plotted
 178 here) and $O + e$ (orange line).

179

180 As displayed in Figure 2, the observed ratio of the 135.6 nm / 130.4 nm emission line brightness varies
181 between 3.0 and 0.5 and was interpreted as a signature of the mixture of H₂O or O relative to O₂. Roth
182 et al. (2021) also suggested that the contribution to these emission lines from electron impact on
183 atomic oxygen was negligible on the disk but can explain the observed decrease in the 135.6 nm /
184 130.4 nm ratio above the limb (at radial distance > 1 R_G in Figure 2).

185 As shown in Figure 2, the best observations in terms of signal noise ratio were obtained when
186 Ganymede was at a phase angle of 98° - 111° (panel a) and 289° - 300° (panel d) (Roth et al. 2021).
187 Adding two other sets of observation allow us to highlight the orbital variability of Ganymede's
188 atmosphere. The 135.6 nm / 130.4 nm emission intensity ratio at the center of the disk (all pixels inside
189 < 0.5 R_G) is lower than ~1.0 at a phase angle of 289° - 300° (panel d), i.e. when the trailing hemisphere
190 is observed. It is slightly higher with values around 1-1.5 on the subjovian (335°- 340°, panel b) and
191 antijovian sides (173°-177°, panel c) and peaking at a value around 2.0 at a phase angle of 98° - 111°
192 (panel a, wake or leading hemisphere). If interpreted with the H₂O abundance reducing the ratio, the
193 observations of a systematically lower ratio at the four orbital positions implies that the H₂O
194 atmosphere is not transient but constantly present. The value of the oxygen emission ratio is around
195 2.5 at the limb at all four orbital positions.

196 We note that the propagated uncertainty of the OI ratio near the disk center in the profiles of the
197 newly added images is particularly high, allowing in principle for values consistent with (almost) only
198 O₂ in the atmosphere. However, when integrating all pixels within 0.8 R_G for the phase angle 335°-
199 340° images (panel b, corresponding to the first 2 radial bins), we find a OI ratio of 1.4 ± 0.8 , which is
200 slightly outside the 1-sigma bounds for a pure O₂ atmosphere. Integrating over all pixels withing 0.6
201 R_G for the phase angle 173° - 177° image (panel c, ~2.4 bins), the OI ratio of 1.1 ± 0.5 is inconsistent
202 with pure O₂ at a 2-sigma level. Thus, also only marginally significant, the radial trend in the OI ratio
203 found by Roth et al. (2021) is also present in the new two datasets.

204 The 2D images of the emission brightness might help us to explain this variability, with auroral regions
205 closer to the center of the disk at $98^\circ - 111^\circ$ and $173^\circ - 177^\circ$ than at $289^\circ - 300^\circ$ and $335^\circ - 340^\circ$. As
206 shown in Marconi (2007), Ganymede's atmosphere is probably composed of H_2O and O_2 and of their
207 products, with a denser O_2 atmosphere in the polar auroral regions and an H_2O atmosphere essentially
208 produced by sublimation around the subsolar region. In another way, at phase angles of $98^\circ - 111^\circ$, the
209 auroral regions are close to the center of the apparent disk, that is, to a region dominated by H_2O
210 leading to a low ratio of the two O emission lines. At 177° , the auroral regions are close to the limb far
211 from the subsolar region, in a region of the exosphere dominated by O_2 leading to a higher ratio of
212 these two O emission lines.

213

214 In order to properly compare observation and simulation, there are three effects that should be
215 considered because they can degrade the spatial resolution when observing Ganymede with HST/STIS:

- 216 • the pixel resolution of the instrument which is about 80 km,
- 217 • the PSF-smearing of about 2-2.5 pixels,
- 218 • the spectral smearing due to the dispersion included in the telescope setup. This will be small
219 and not distinguishable from spatial effects. We neglect the effects in our modelling.

220 The first two effects are taken into account by projecting the simulated image on a grid with 80 km
221 resolution and then convolving this with a 2D Lorentzian with a FWHM of 2.5 pixels.

222

223 **III Exospheric Global Model**

224 **III.1 Description of the model**

225 The Exospheric Global Model (EGM) is a 3D time dependent Monte Carlo model that describes the fate
226 of atmospheric species ejected from Ganymede's surface, moving under the influence of Ganymede
227 and Jupiter gravity fields, being absorbed or reejected when reimpacting the surface and eventually

228 ionized or dissociated by photon and electron impacts. All products of water and O₂ are described, that
 229 is, H₂O, H, H₂, O, O₂ and OH. EGM can also describe the effects of collision between these species in
 230 the case of weakly dense atmosphere but in the following we will present simulations performed by
 231 neglecting collisions between atmospheric species. Indeed, as explained in Leblanc et al. (2017),
 232 collisions have a limited impact on the 3D large scale structure of the atmosphere and would not
 233 change the conclusions of this present work. All details regarding EGM can be found in Leblanc et al.
 234 (2017). EGM is time dependent so that it allows to follow the trajectory of the exospheric particles all
 235 along Ganymede rotation around Jupiter. It therefore takes into account the centrifugal and Coriolis
 236 forces applied on these particles due to Ganymede rotation in Jupiter frame and the variations of the
 237 solar illumination (including the shadow induced by Jupiter) during Ganymede's orbit.

238 With EGM, we reconstruct in 3D the density, bulk velocity and temperature of all neutral species
 239 around Ganymede. In order to reconstruct the emission intensity, we consider the various electron
 240 and photon induced reactions that could produce the 130.4 nm, 135.6 nm or 121.6 nm emissions. In
 241 the case of electron impact induced emission excitation, we considered various laboratory
 242 measurements as listed in the fourth column of Table 1. The calculated emission rates at an energy of
 243 100 eV are close to the ones used in Roth et al. (2021), as displayed in the second and third columns
 244 of Table 1, except for electron impact on O impact leading to 135.6 nm emission for which we used
 245 different cross sections than in Roth et al. (2021). For photon impact emission excitation, we used
 246 previously published rates as indicated in Table 1.

Reactions	Rate for electrons at 100 eV (Roth et al. 2021)	Rate for electrons at 100 eV (This work)	Reference
O ₂ + e → 1356 Å	3.7×10 ⁻⁹ cm ³ s ⁻¹	3.8×10 ⁻⁹ cm ³ s ⁻¹	Kanik et al. (2003)
O ₂ + e → 1304 Å	1.57×10 ⁻⁹ cm ³ s ⁻¹	1.72×10 ⁻⁹ cm ³ s ⁻¹	
O + e → 1356 Å	0.195×10 ⁻⁹ cm ³ s ⁻¹	0.24×10 ⁻¹⁰ cm ³ s ⁻¹	Tayal et al. (2016)

$O + e \rightarrow 1304 \text{ \AA}$	$4.84 \times 10^{-9} \text{ cm}^3 \text{ s}^{-1}$	$5.38 \times 10^{-9} \text{ cm}^3 \text{ s}^{-1}$	Johnson et al. (2005)
$H_2O + e \rightarrow 1304 \text{ \AA}$	$0.16 \times 10^{-9} \text{ cm}^3 \text{ s}^{-1}$	$0.19 \times 10^{-9} \text{ cm}^3 \text{ s}^{-1}$	Makarov et al. (2004)
$H_2O + e \rightarrow 1356 \text{ \AA}$	$0.32 \times 10^{-10} \text{ cm}^3 \text{ s}^{-1}$	$0.37 \times 10^{-10} \text{ cm}^3 \text{ s}^{-1}$	Rate at 130.4 nm divided by 5 (Roth et al. 2021)
$H_2 + e \rightarrow 1216 \text{ \AA}$	Not available	$3.2 \times 10^{-9} \text{ cm}^3 \text{ s}^{-1}$	Ajello et al. (1995)
$H_2O + e \rightarrow 1216 \text{ \AA}$	Not available	$4.2 \times 10^{-9} \text{ cm}^3 \text{ s}^{-1}$	Makarov et al. (2004)
Reactions	Excitation rate		Reference
$H_2O + h\nu \rightarrow H + H +$ $O \ 1216 \text{ \AA}$	$1.4 \times 10^{-10} \text{ s}^{-1}$		Roth et al. (2014)
$H + h\nu \rightarrow 1216 \text{ \AA}$	$7.29 - 11.8 \times 10^{-5} \text{ s}^{-1}$		Alday et al. (2017)
$O + h\nu \rightarrow 1304 \text{ \AA}$	$4.0 \times 10^{-7} \text{ s}^{-1}$		Roth et al. (2021)

247 **Table 1:** Reactions and rates used to calculate the emission intensity at 1304, 1356 and 1216 Å.

248 In Leblanc et al. (2017), we discussed two scenarios for the production of H₂O. One case with low
249 sublimation rate (hereafter the dry exospheric case) is inconsistent with the H₂O/O₂ ratios from Roth
250 et al. (2021) for O₂ column densities higher than $1 \times 10^{13} \text{ cm}^{-2}$, as generally assumed to be the case for
251 Ganymede (Hall et al. 1998, Johnson et al. 2004). The second case used nominal sublimation rate as
252 calculated from Fray and Schmitt (2009) parametrization of the sublimation of water ice at very low
253 pressure and cold temperature. Using the nominal sublimation rate scenario, we here simulate five
254 consecutive orbits of Ganymede around Jupiter following around 2×10^6 test-particles at each time step
255 of 0.25 s. Few hundred thousand test-particles were used to describe each of the 6 species, namely,
256 H, H₂, O, OH, H₂O and O₂ with weight values between 10^7 to 10^{16} (number of real particles represented
257 by each test-particle). The macroscopic quantities like density, velocity, temperature, escape flux and
258 reabsorbed surface flux are reconstructed on a 100 (along the radial direction) \times 50 (along the polar
259 direction) \times 100 (along the azimuth direction) spherical grid. A typical run lasts one to two weeks on

260 64 CPUs. Four orbits are needed in order to reach a steady solution with no significant difference in
261 the 3D reconstructed macroscopic parameters between the two last orbits.

262 The characteristics of the electron population at the origin of the auroral emissions remain poorly
263 constrained by observation. Roth et al. (2021) assumed an effective averaged homogeneous electron
264 density with values between 20 and 30 cm^{-3} , an electronic temperature of 100 eV and global O_2
265 abundances of $\sim 3 \times 10^{14} \text{ O}_2/\text{cm}^2$, which yields effective 135.6 emission brightnesses primarily produced
266 by impact of electrons on O_2 (see Figure 3) in the range of the observed values. As discussed in Carnielli
267 et al. (2020a), the original $10^{14} - 10^{15} \text{ O}_2/\text{cm}^2$ suggested by Hall et al. (1998) is based on the upper limit
268 set by a stellar occultation observation performed by Voyager 1 (Broadfoot et al. 1979) which
269 suggested actually an upper limit at $2.5 \times 10^{15} \text{ cm}^{-2}$ (Carnielli et al. 2020a). Carnielli et al. (2020a)
270 reconstructed the ionospheric density, compared the resulting density to the G2 flyby measurements
271 for the case of a dry exosphere (Leblanc et al. 2017) and concluded that both exospheric content and
272 electron ionization rate might have been underestimated in previous modelling (Marconi 2007;
273 Leblanc et al. 2017) illustrating the difficulty to derive from the auroral emission observations an
274 accurate estimate of Ganymede's atmospheric content without knowing the electron density and
275 temperature. Eviatar et al. (2001) using a simple auroral model (or more specifically, the electron
276 energy spectral flux measured by Galileo over the auroral region) suggested that the electron density
277 responsible for Ganymede's auroral emissions should be closer to a few hundred cm^{-3} rather than few
278 ten of cm^{-3} . Such a much larger electron density would mechanically imply a much less dense
279 exosphere in the auroral regions to explain the observed auroral brightnesses except if the electron
280 temperature is significantly smaller than supposed by these authors.

281 In the following, we chose to use an electron population at 100 eV. A uniform reaction rate
282 corresponding to the rate displayed in Table 1 multiplied by an electron density of 20 cm^{-3} is assumed
283 everywhere except over the auroral ovals. A locally increased reaction rate is set over the latitudes
284 $\pm 10^\circ$ of the OCFB (see Figure 3 of McGrath et al. 2013 and Figure 3 of Leblanc et al. 2017) and
285 corresponds to the rate displayed in Table 1 multiplied by an electron density of 70 cm^{-3} . The $\pm 10^\circ$ was

286 chosen to reproduce roughly the observed latitudinal width (c.f. Musacchio et al. 2017, their figure 9)
 287 and corresponds to the current structure in Ganymede’s magnetosphere as modelled by Jia et al.
 288 (2009). The ejection mechanisms at the origin of Ganymede’s exosphere are also constrained using
 289 this same separation between open and close field line regions as described in Leblanc et al. (2017).

290

291 III.2 Ganymede’s exosphere as modelled by EGM

292 Table 2 provides the surface ejection rate for the 7 species described in EGM for the nominal
 293 sublimation rate and sputtering conditions. With the exception of water molecules which can be
 294 ejected by sublimation, most of the species are ejected from the surface by sputtering or radiolysis
 295 induced ejection. The typical rates are close to the ones used in Marconi (2007). When comparing the
 296 source rates with the neutral escape rates, we can see that loss and source terms are never equal
 297 which implies that surface reabsorption, photon and electron impact dissociation and photon and
 298 electron impact ionization are important loss mechanisms. Vorburger et al. (2021) recently published
 299 a detailed modelling of Ganymede’s exosphere. They concluded that Leblanc et al. (2017) sputtering
 300 water rate was up to two orders larger than the ones of other models. It is unclear what the origin of
 301 these discrepancies is, our reconstructed yield being based on Cassidy et al. (2013) analysis derived
 302 from a large set of laboratory measurements.

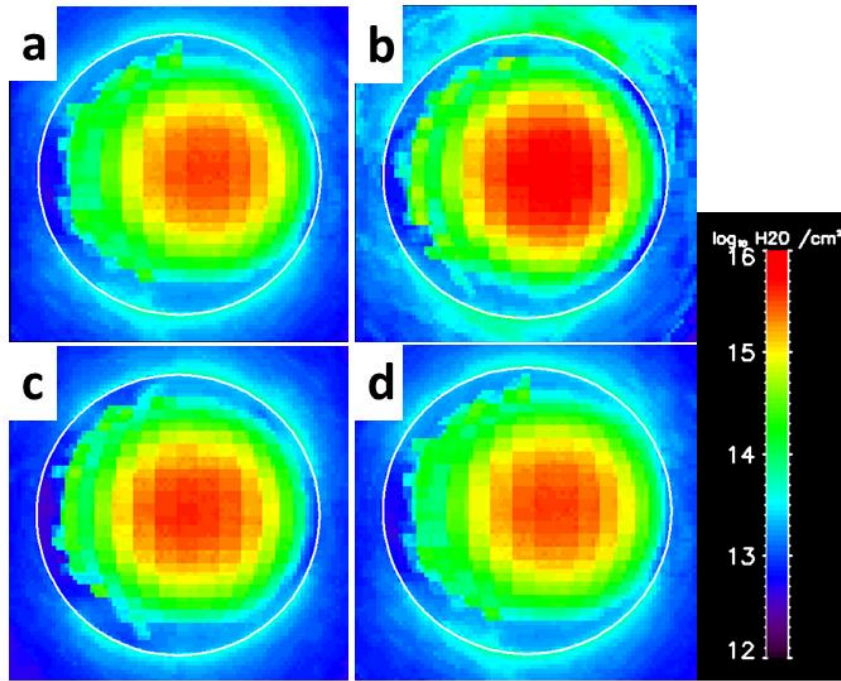
Species		H	H ₂	O	OH	H ₂ O		O ₂
Source		Sputtering	Sputtering	Sputtering	Sputtering	Sputtering	Sublimation	Sputtering
Rate (s ⁻¹)	Surface ejection	2.0×10 ²⁵	8.3×10 ²⁶	1.0×10 ²⁵	1.0×10 ²⁵	4.0×10 ²⁷	8.0×10 ²⁹	4.4×10 ²⁶
	Escape	2.9×10 ²⁶	2.7×10 ²⁶	1.0×10 ²⁶	4.0×10 ²⁵	7.0×10 ²⁶		4.4×10 ¹⁵

303 **Table 2:** Simulated source and neutral escape rates (average values on 2 consecutive orbits)

304 In the case of the atomic H exosphere, the neutral escape rate is 10 times larger than the sputtering
 305 rate which is due to the fact that most of the H atoms are produced from the dissociation of H₂O and
 306 H₂. Moreover, dissociation produces H atoms with enough energy to be lost by neutral escape. A small

307 fraction of these H atoms is also reabsorbed by the surface or ionized. In the simulation, H₂ is not
308 reabsorbed by the surface by assumption (see Leblanc et al. 2017), so that H₂ molecules either escape
309 as neutral particle, are dissociated or are ionized. Oxygen atoms can be sputtered from the surface but
310 are also the products of the dissociation of O₂ and H₂O. A large proportion of the O atoms are
311 reabsorbed in the surface. In the same way, OH is either ejected from the surface by sputtering or
312 produced from the dissociation of H₂O exospheric molecules. The main source of the H₂O exosphere
313 is sublimation, the sputtering rate being of less than one percent of the sublimation one. Most of the
314 H₂O molecules ejected from the surface are reabsorbed in the surface. Contrary to the other
315 exospheric species, O₂ is too heavy to escape Ganymede gravity as neutral so that its ejection rate is
316 balanced by the dissociation and ionization rates. Numerically, a simulation of more than 4 orbits is
317 needed to reach a steady state between loss and source for this species.

318 In Figures 4 and 5, we display how Ganymede's H₂O and O₂ exospheric column densities would be seen
319 from the Earth at the four positions of HST/STIS observations described in Figure 1. As expected and
320 described in many past publications (see example, Marconi 2007; Plainaki et al. 2015; Leblanc et al.
321 2017; Plainaki et al. 2020), the H₂O exosphere is spatially organized compared to the O₂ exosphere,
322 with a peak near the subsolar point for the H₂O whereas the O₂ column density peaks around the limb
323 with slightly larger values near the poles. As explained in Leblanc et al. (2017), Oza et al. (2019) and
324 Johnson et al. (2019), Ganymede's orbital motion leads to a slightly shift of the H₂O peak towards the
325 dusk side.



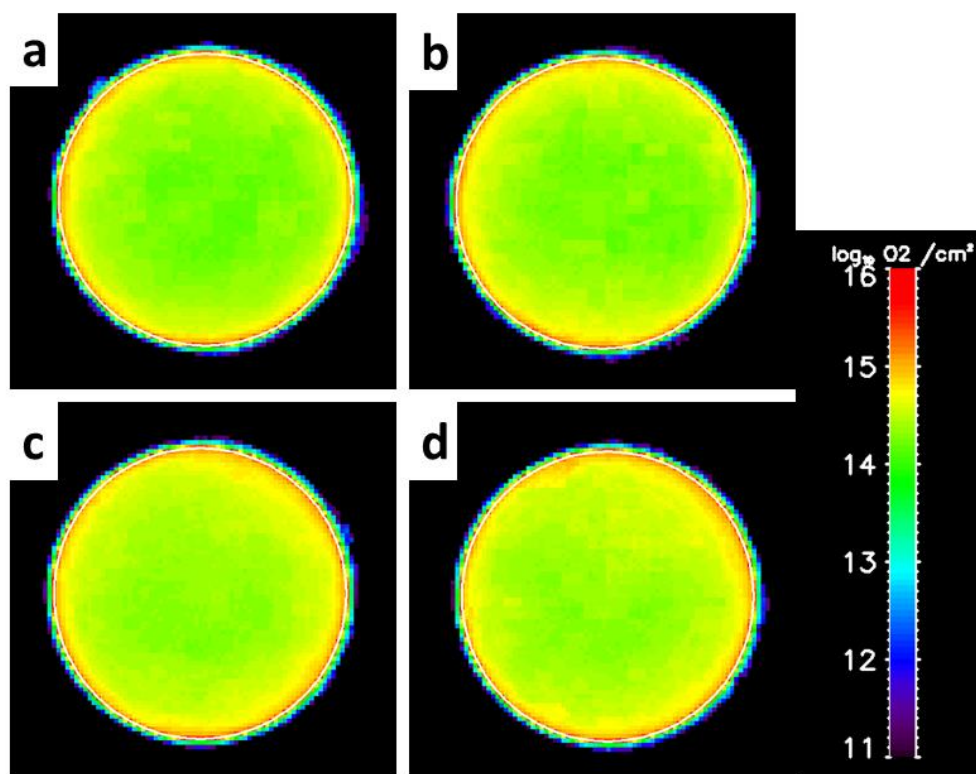
326

327 **Figure 4:** Simulated column densities of the H₂O exospheric component (in log₁₀ cm⁻³) at the four
 328 positions of Figure 1 in the nominal simulation case. Panel a: phase angle of 98°-111°. Panel b: phase
 329 angle of 335°-340. Panel c: phase angle of 173° - 177°. Panel d: phase angle between 289° - 300°. The
 330 subsolar point is at the center of each panel. Dawn is on the left of each panel, the North being towards
 331 the top. Ganymede limb is represented by the white circle.

332

333 Whereas we observe a significant change with respect to Ganymede orbital positions in the H₂O
 334 exosphere as seen from the Earth, the O₂ exosphere does not appear to vary in terms of global
 335 distribution. The water orbital variability is related to the change in surface albedo between leading
 336 and trailing sides of Ganymede (Spencer 1987) leading to a variation between 146 (maximum on the
 337 trailing side) to 142 K (minimum on the leading side) of the subsolar surface temperature and to an
 338 order of magnitude variation of the sublimation rate (see Figure 2 in Leblanc et al. 2017). The maximum
 339 H₂O column density around the subsolar region reaches values of few 10¹⁵ H₂O/cm² near the surface
 340 (and a peak density around 10⁹ H₂O/cm³ at the surface with atmospheric temperature close to the
 341 surface one up to 400 km in altitude) and decreases to a plateau at 10¹³ H₂O/cm² from 500 km to few

342 thousands km in altitude (corresponding to temperature around 2000 K above 800 km). These two-
 343 slope profile is related to the two main sources of H₂O sputtering and sublimation (Table 2). The only
 344 change that can be inferred from the 2D images of the O₂ column density is due to the latitudinal
 345 extension of the polar regions which is closer to the equator when the leading side of Ganymede is
 346 illuminated (Figures 2 panels a and c) with respect to the trailing side illuminated hemisphere. The O₂
 347 column density peaks at a value of 10¹⁵ O₂/cm² at the surface (and a density of 10⁸ O₂/cm³) and
 348 decreases by three to four orders of magnitude within the first 100 km in altitude.



349

350

Figure 5: Same as in Figure 4 but for the O₂ column density.

	Phase angle 98°- 111°	Phase angle 173° - 177°	Phase angle 289° - 300°	Phase angle 335°-340°
H	2.5×10 ⁺¹¹	1.2×10 ⁺¹¹	2.8×10 ⁺¹¹	2.2×10 ⁺¹¹
H ₂	5.6×10 ⁺¹⁴	6.1×10 ⁺¹⁴	5.0×10 ⁺¹⁴	4.6×10 ⁺¹⁴
H ₂ O	5.6×10 ⁺¹⁴	6.4×10 ⁺¹⁴	1.3×10 ⁺¹⁵	1.0×10 ⁺¹⁵

O	1.6×10^{12}	2.5×10^{12}	1.0×10^{12}	1.1×10^{12}
O ₂	4.3×10^{14}	4.3×10^{14}	3.6×10^{14}	3.7×10^{14}
OH	1.5×10^{12}	1.5×10^{12}	1.2×10^{12}	4.7×10^{12}

351 **Table 3:** *Simulated disk averaged column densities in cm⁻² for the nominal sublimation and sputtering*
352 *rate conditions*

353 As illustrated in Figures 4, 5 and Table 3, there is some orbital dependency of Ganymede's exosphere
354 which are essentially driven by the leading/trailing variation of the albedo which controls the
355 sublimation rate of the H₂O and in a lesser way the efficiency of the sputtering (Cassidy et al. 2013).
356 Whereas the O₂ and H₂ average column densities do not change significantly along Ganymede's orbit,
357 the H₂O exosphere column density displays a clear variation. According to Table 3, Ganymede's
358 exosphere is always dominated by water molecules in an average over the full disk.

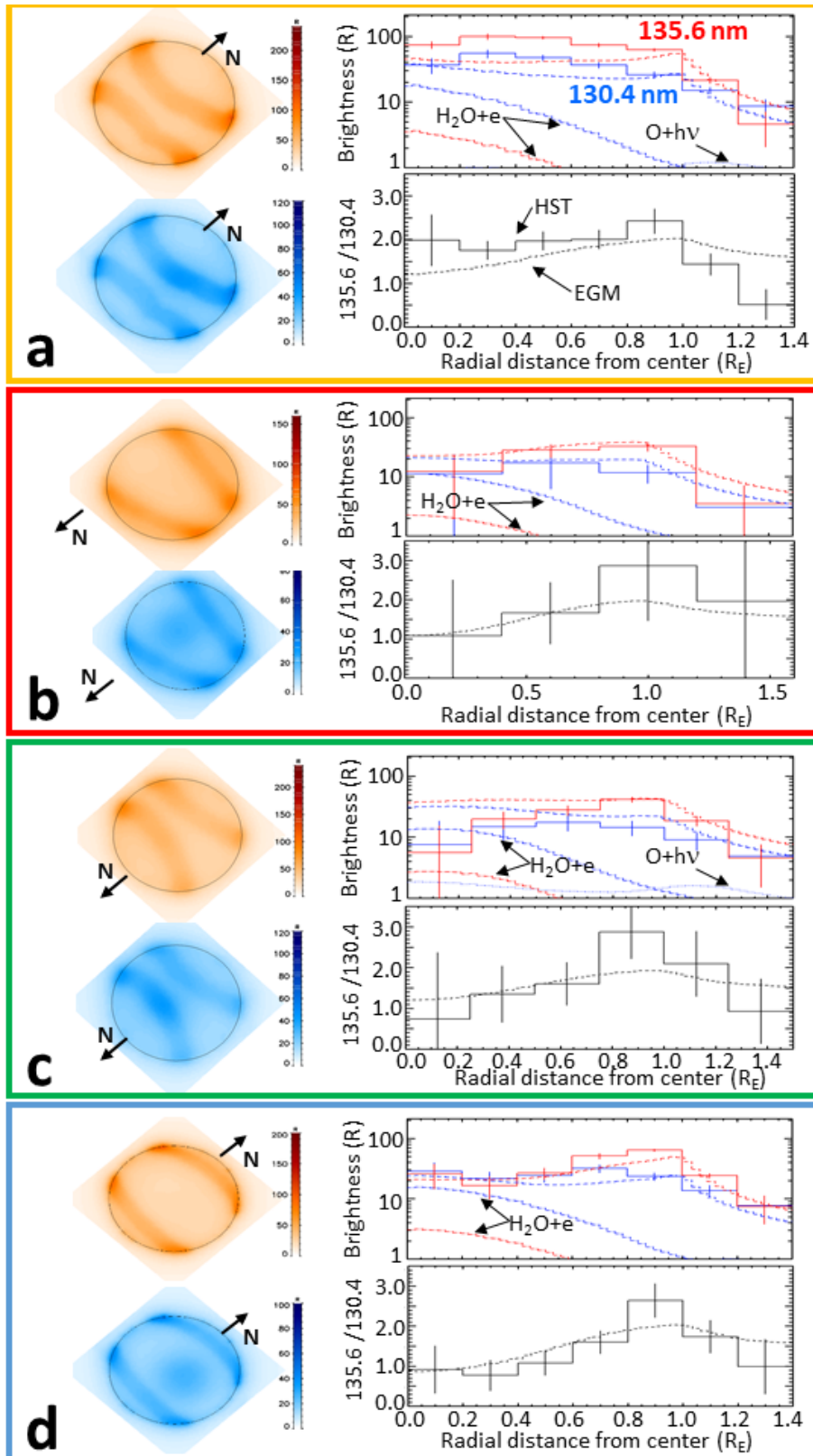
359

360 **IV Comparison with HST observations**

361 *IV.1 Reconstructed oxygen emissions*

362 All together, the agreement between observation and simulation using the nominal sublimation rate
363 (section III.2) as displayed in Figure 6 is remarkably good considering that we did not make any change
364 of the exospheric model and used a fixed temperature and density of the electrons responsible for the
365 auroral emission (section III.1). There are however still several discrepancies between the simulated
366 profiles (right panels in each rectangle) which could be either due to the electron population
367 description or due to the exospheric description as discussed in the following.

368



369

370 **Figure 6:** Comparison between observation of Ganymede's atmospheric emission by HST/STIS and EGM
 371 simulation. Each panel corresponds to one date. a 2010-11-19, phase angle of 98° - 111° (Roth et al.
 372 2021). b: 2003-11-30, phase angle of 335° - 340° (McGrath et al. 2013). c: 2017-02-02, phase angle of

373 173°-177°. d: 1998-10-30, phase angle between 289° - 300° (Roth et al. 2021). Each panel surrounded
374 by a rectangle which colour corresponding to Figure 1 circle colours is composed of the simulated
375 images of the 1356 Å (red) and 1304 Å (blue) brightness intensities, of the radial profile from the center
376 of the disk up to around half a radius above the limb of the emission brightness intensity for these
377 wavelength (top right panel in each rectangle with in solid line, HST/STIS observations, in dashed lines,
378 EGM reconstructed emission intensity, in dashed-dotted lines, EGM emission intensity from H_2O+e
379 reaction and in dotted line, EGM emission intensity from $O+h\nu$ reaction) and of the ratio of these two
380 emission lines 1356 emission intensity divided by 1304 emission intensity (bottom right panel in each
381 rectangle).

382

383 Starting from panel a, at a phase angle of 98°-111°, that is looking to Ganymede when its leading side
384 faces the Sun, the measured 135.6 nm emission (red solid line) is underestimated by 50% by the
385 simulation on the disk (below a radial distance of $0.8 R_G$). The observed 130.4 nm emission (solid blue
386 line) is also slightly underestimated. The 135.6 nm emission being produced by electron impact on the
387 O_2 molecule (the dashed-dotted red line corresponds to the emission intensity produced by electron
388 impact on H_2O molecules which is then one order smaller), a 50% denser O_2 exosphere on the
389 illuminated leading side or an electron density larger by 50% (that is an electron density $\sim 100 \text{ cm}^{-3}$ in
390 the auroral regions) would lead to a much better reproduction of the observations close to the center
391 of the disk. At the limb (above $1 R_G$), the ratio of the two observed emission lines decreases down to a
392 value around 0.5, showing either an increase of the amount of H_2O molecules at the origin of these
393 emissions or an increase of the atomic oxygen abundance. Roth et al. (2021) suggested that the oxygen
394 atoms should get more abundant in the exosphere at higher altitude being among the less massive
395 species. Clearly, if it is the case, the model underestimates this population. Oxygen atoms can come
396 either from the dissociation of the O_2 and H_2O or directly from the surface sputtering. Since increasing
397 the O_2 and H_2O densities, in particular close to the limb, would lead to a discrepancy with the

398 observations, the most plausible explanation is that the flux of O atoms sputtered from the surface is
399 underestimated by the model. We therefore tested much larger ejection rate by sputtering of the O
400 atoms, by up to a factor 100, and simulated an exosphere with emissions closer to the ones reported
401 in Figure 2 but still not matching the observed emission brightness ratio at $1.3 R_G$ from the limb. The
402 reconstructed 2D images of the emission brightness as displayed in Figure 6a (left) reproduced the
403 shape of the auroral emissions, logically since we imposed it arbitrarily in our reconstruction of these
404 emissions, through the increase in electron density around the OCBF (see section III). We also
405 simulated a limb asymmetry between dawn and dusk, an asymmetry due to the asymmetry of the
406 exosphere as seen from the Earth. Such asymmetry in the auroral emissions might be also related to
407 the electron current system as discussed by Musacchio et al. (2017).

408 At a phase angle around $335^\circ - 340^\circ$ (panel b in Figure 6), the Sub-Jovian hemisphere of Ganymede
409 faces the observer. For such case, the model results are in rather good agreement with the
410 observation, the emission brightness intensities of the two emission lines and their ratio being
411 reproduced by the model within the uncertainties of the observation. A similar excellent agreement
412 between simulation and observation is also obtained at a phase angle of $289^\circ - 300^\circ$ (panel d). However,
413 at $0.9 R_G$ from the center of the disk, the observed ratio reaches a value above 2.5. Even with a pure
414 O_2 exosphere, maximum values around 2 would be produced according to Figure 3d, making a ratio of
415 2.5 very unlikely with only a mixture of H_2O and O_2 .

416 The comparison between simulated emission brightness intensity and observed ones in panel c (phase
417 angle of $173^\circ - 177^\circ$) displays significant discrepancies. Close to the center of the disk, the model
418 calculated an emission brightness much more intense than observed, by a factor 6 for the 135.6 nm
419 emission and a factor 4 for the 130.4 nm emission. At this orbital position, Ganymede's anti-Jovian
420 hemisphere faces the observer. A potential reason for the observed decrease in the emission
421 brightness intensity close to the center of the disk at such orbital position might be therefore related
422 to the dependency of the current system at the origin of these auroral emissions with respect to the

423 ram/wake orientation and Jovian/Anti-Jovian hemisphere, a dependency that we did not consider
424 when adopting constant density and energy of the electron in the auroral bands. A smaller density of
425 the electron at the origin of these emissions would lead to a less intense emission intensity but to a
426 similar value of their ratio. At the limb, the observed emission lines have similar intensities, leading to
427 a ratio close to one. The simulation predicts a ratio close to 1.5 which is consistent with the observation
428 when considering the uncertainty on the observed ratio. At $0.8 R_G$ from the center of the apparent
429 disk, this same ratio reaches a value of 2.8 ± 0.7 . If real, it would suggest a mechanism for the production
430 of these emissions which is not taken into account in our model.

431 To summarize, the nominal sublimation model of Ganymede's exosphere convolved with the simple
432 description of the population of electron at the origin of the observed emission leads to a good
433 agreement with the observation on the side of the orbit when Ganymede trailing hemisphere is facing
434 the Sun. We obtained a less good agreement on the other side. In the exospheric model, the only
435 difference taken into account between these two portions of the orbit is related to the change of the
436 wake/ram angle with respect to the subsolar/anti-solar direction. The most probable origin of this
437 discrepancy is related to the simple description of the electron population leading to these auroral
438 emissions. This population has been shown to be variable and dependent on the wake/ram, Sub-solar
439 – anti-jovian axis and to the sub-solar direction (Jia et al. 2009; Sauer et al. 2015). As a matter of fact,
440 Carnielli et al. (2020a) reconstructed the ionosphere of Ganymede using Leblanc et al. (2017) dry
441 exospheric model and concluded that the density of ionising electrons is denser than previously
442 inferred from Galileo (Carnielli et al. 2019) at (or extrapolated to) Ganymede's orbit so that the
443 electron impact ionization frequency should be increased by a factor 4 in the anti-Jovian hemisphere
444 for the G2 flyby conditions. As a matter of fact, recent radio-occultation observations performed during
445 JUNO flyby of Ganymede suggest an electron density close to the surface of $2000 \pm 500 \text{ cm}^{-3}$ in the open
446 magnetic field regions of Ganymede magnetosphere (Buccino et al. 2022). A higher ionisation
447 frequency is also consistent with our conclusions that to reproduce the observed emission profiles
448 above the limb, a higher electron impact dissociation rate of O_2 is needed. Carnielli et al. (2020a) also

449 concluded that the O₂ density in the polar regions should be increased by a factor 10 with respect to
450 the dry scenario (Table 3). The nominal sublimation scenario used here leads to H₂O average column
451 densities 30 to 100 times denser than in the dry scenario (Leblanc et al. 2017). However, a nominal
452 sublimation rate scenario might be not enough to reproduce Galileo electron density at high latitudes,
453 since the H₂O exosphere is essentially concentrated in the sublimation equatorward region. Moreover,
454 a 10 times denser O₂ exosphere convolved with a higher electron impact rate, would probably lead to
455 a significantly larger 135.6 nm / 130.4 nm ratio in the auroral regions in disagreement with the
456 observations (Figure 6). Without a detailed knowledge of the electron density and temperature in the
457 open field lines regions, it is therefore not realistic to conclude firmly on how to reconcile measured
458 electron density and auroral emission intensities. We note, however, that the 135.6 nm / 130.4 nm
459 ratio for O₂ is similar within the relevant electron temperatures range (e.g. Kanik et al. 2003 and Figure
460 3d). If the ratio for H₂O is similarly insensitive to the temperature as supposed in Figure 3d, firm
461 conclusions are possible without exact knowledge of the absolute excitation and brightnesses.

462 As discussed before, the ratio of the two measured emission lines above the limb suggests an
463 underestimate of the O population by EGM in this region. We simulated much larger sputtering rate
464 of the O atoms (by a factor 100) from the surface without changing significantly the simulated ratio
465 displayed in Figure 6. The main reason is that the main source of the O exospheric population is not its
466 sputtering from the surface but the dissociation of O₂ and H₂O. We therefore performed a simulation
467 with an electron impact rate increased by a factor 2.0 in the open field lines region (equivalent to
468 increase the electron density by a similar factor). However, increasing the electron impact dissociation
469 also leads to a lower density of both molecules and therefore a smaller brightness intensity at 130.4
470 and 136.6 nm. We had therefore to increase by a factor 1.8 the sputtering rate of both O₂ and H₂O to
471 compensate the increase in their dissociation rate to fit the observed emission brightness. We also had
472 to increase the sputtering rate for O and H with respect to the one of O₂ by a factor 40 in order to
473 retrieve emission brightness ratio above the limb close to the ones observed by HST. With such
474 increase of the sputtering rate of H and O, sputtering is equivalent to the dissociation of O₂ and H₂ as

475 source for these two exospheric species. The density for these two species significantly increased by
476 more than an order of magnitude in the case of H and by a factor 2 to 3 in the case of the O exosphere.
477 In that case, the simulated O column density is marginally larger than the upper limit set by Roth et al.
478 (2021) for the column density by a factor 2.5. The other species, namely H₂, O₂, H₂O and OH, remains
479 almost unchanged with respect to the nominal species.

480

481 *IV.2 Reconstructed H emission*

482 Lyman α emission from Ganymede's atmosphere was detected for the first time by Galileo (Barth et
483 al. 1997) and later confirmed from HST by Feldman et al. (2000). Recently, Alday et al. (2017) provided
484 a detailed analysis of four sets of HST observations obtained between 1998 and 2014. These authors
485 estimated the emission brightness from Ganymede's corona (outside from the apparent disk) as
486 ranging from 0 to 450 R for a phase angle between 77.9° and 103.5° (average emission of 215±66 R),
487 from 110 to 310 R for a phase angle between 269.3° and 291.8° (average emission of 180±52 R). As
488 discussed in Alday et al. (2017), the globally lower emission intensities of the Lyman α emission
489 obtained in 2014 with respect to the other set of observations obtained in 1998, 2010 and 2011 are
490 probably due to strong absorption of the emission by the geocorona. Excluding these 2014
491 observations, the Lyman α emission brightness between 90.1° and 103.5° is 328±159 R and at 291.8°
492 is 310 R.

493 In order to predict brightnesses, we simulated the emission brightness at Lyman α using the various
494 possible excitation processes described in Table 1 for the nominal exosphere case. At a phase angle of
495 98° - 111°, the emission brightness intensity at Lyman α was simulated as being equal to 170 Rayleigh
496 on the apparent disk and 47 Rayleigh outside. On the disk, H₂O electron impact emission dominates
497 with 100 Rayleigh induced by this process and 50 Rayleigh is associated with H₂ electron impact.
498 Outside of the disk, H₂O electron impact induces only 9 Rayleigh of emission intensity and 25 Rayleigh
499 is produced by H₂ electron impact. Very similar values are simulated at a phase angle of 289° - 300°.

500 These H Lyman-alpha aurora intensities are not discernible from the other sources in the HST
501 observations and therefore not detectable. For resonant scattering by H atoms, we get intensities on
502 the order of 10-20 Rayleigh for our simulations. With respect to the reported emission intensity in the
503 extended corona outside of the disk with peak brightness near the moon of ~300 R (Alday et al. 2017),
504 our simulated intensities are therefore an order of magnitude too low.

505 The only way to increase the simulated emission intensity would be to increase the density in H atoms.
506 exospheric H atoms are produced either from direct sputtering from the surface or coming from the
507 dissociation of H₂O and H₂. Increasing the H₂O or H₂ dissociation rate is possible by increasing the H₂O
508 or H₂ density but this would lead to a disagreement between simulation and observation regarding the
509 OI 130.4 nm and 135.6 nm emission line profiles (Figure 6). It is also possible that the dissociation
510 frequency used in our simulation for these two molecules is underestimated because of a higher
511 electron density or temperature. Increasing the electron energy would lead to a small increase of the
512 electron impact dissociation, the typical electron impact dissociation cross section with respect to the
513 electron energy forming a plateau above 20 eV for H₂+e → H + H (Dalgarno et al. 1999) or peaking
514 around 100 eV for H₂O+e → H+OH and H₂O + e → H+H+O (Song et al. 2021). We performed a
515 simulation where the electron impact rate is increased by a factor 2 through an increase of the electron
516 density in the open field lines region, combined with a sputtering rate of the H atoms increased by a
517 factor 72. In that case, between 98° and 111°, the H density in the corona of Ganymede is increased
518 by a factor 10, leading to a stronger emission intensity from the corona equal to 450 Rayleigh on the
519 disk and of 230 Rayleigh outside the disk (with 20 Rayleigh produced by electron impact on H₂ and 200
520 by resonant scattering on H atoms). At a phase angle of 289° - 300°, the H corona is also increased by
521 a factor 10 leading to an emission brightness of 300 Rayleigh on the disk and of 180 Rayleigh outside
522 the disk (with 20 Rayleigh produced by electron impact on H₂ and 160 by resonant scattering on H
523 atoms). Therefore, as concluded in the case of the oxygen atoms, a sputtering rate of H atoms from
524 Ganymede surface increased by almost two orders of magnitude and a factor two increase of the

525 electron impact dissociation of H₂ and H₂O with respect to the nominal value are needed to reproduce
526 the brightness intensity of the Lyman α extended exosphere of Ganymede.

527

528 **VI Conclusion**

529 Ganymede's atmosphere is thought to be composed of water molecules and its products (in particular
530 O₂), thanks to several set of observations from Galileo and Hubble Space Telescope (HST) and to
531 modelling (see Roth et al. 2021 for more details). Ganymede's atmosphere is probably unique in our
532 solar system, in the sense, that it is not exactly a surface bounded exosphere as defined by Stern (1999)
533 but is probably collisional locally. Indeed, it is partly produced by (1) the sublimation of its icy surface
534 around the subsolar point which leads to a water molecular atmosphere locally thick enough to be
535 collisional; and (2) for the rest of its surface, by the permanent bombardment of its surface by the
536 Jovian and ionospheric electrons and ions leading to radiolysis and sputtering (Roth et al. 2021). The
537 observation of Ganymede's atmosphere presented in Roth et al. (2021) provided for the first time the
538 clear evidence of the presence of a thick water molecular atmospheric component as predicted by
539 Marconi (2007). Roth et al. (2021) analysed a set of HST observations with a simple parametric
540 description of Ganymede's atmosphere and derived the amount of water molecule that should be
541 present around Ganymede. A recent study by de Kleer et al. (2023) measured optical oxygen emissions
542 deriving a global upper limit on the H₂O/O₂ ratio below Roth et al. (2021) derived ratios from aperture-
543 integrated emissions brightnesses. Although the authors claim a conflict with Roth et al. (2021) results,
544 they are in fact consistent: the majority of the emissions on the sub-Jovian are located near or above
545 the limb. The globally integrated emission ratio, which de Kleer et al. use, is therefore only
546 representative for this region and the lower line ratio on the disk center and the H₂O abundance there
547 will remain undetected in their data.

548 In this paper, the newly published observations are taken such that the anti-Jovian and sub-Jovian
549 hemispheres are observed, i.e. at intermediate geometries between the previously published leading

550 and trailing side observations (Roth et al. 2021). The new data show that the 135.6 nm/130.4 nm ratio
551 in the Ganymede disk center is also intermediate, i.e., lower on the leading side but higher on the
552 trailing side. This means that the oxygen emission ratio and related molecular abundances appear to
553 be modulated by Ganymede's orbital period. Using a simplified description for the electron to
554 reconstruct the electron impact excitation at the origin of HST observations, we showed that
555 Exospheric Global Model (EGM; Leblanc et al. 2017) provides a rather good agreement with this set of
556 observations obtained at four positions of Ganymede around its orbit. By modelling the orbital
557 variability of the surface radiolysis and sublimation and their dependency with respect to the intrinsic
558 Ganymede's magnetosphere and to the surface temperature, EGM succeeded to provide a consistent
559 description of the origins of Ganymede's exosphere and of its content.

560 We found slightly smaller amount of water than Roth et al. (2021), with an average disk column density
561 between $0.5 \times 10^{+15}$ H₂O/cm² when the leading hemisphere of Ganymede is illuminated and $1.3 \times 10^{+15}$
562 when it is the trailing hemisphere. The H₂O atmosphere density on the sub-Jovian and anti-Jovian sides
563 is in between these values, consistent with the observations. The O₂ atmosphere is less variable with
564 an average disk column density around $4.0 \times 10^{+14}$ O₂/cm², a relatively low abundance with respect to
565 previous analysis (Hall et al. 1998). Our analysis also suggests that the spatial distribution of the
566 exosphere should be slightly shifted towards the dusk side on the dayside, in particular for its H₂O
567 component. We also discussed the reconstructed Lyman α emission brightness and compared it to
568 observations (Alday et al. 2017) and showed that the model significantly underestimates the
569 brightness intensity of this emission line far from Ganymede's surface. As for the oxygen emission lines,
570 we concluded that to reproduce the emission brightness far from the surface, a much higher sputtering
571 rate of the oxygen and hydrogen atoms is needed with respect to the nominal rate used in Leblanc et
572 al. (2017) and previous publications. This higher sputtering rate should be also combined with a two
573 times higher dissociation rate of the exospheric molecules close to Ganymede, suggesting a denser
574 electron population with enough energy to dissociate the exospheric molecules in the open field line
575 regions than supposed in Leblanc et al. (2017).

576 This paper provides the first consistent attempt to reconstruct of the observations that presently
577 constrain Ganymede's exosphere. It also highlights the need to properly take into account the various
578 possible sources of the auroral emissions, in particular the electron population. Without either in-situ
579 measurements to better constrain this electron population, or detailed modelling of the ionosphere
580 and its suprathermal electron component, any analysis of the auroral emissions observed around
581 Ganymede would remain a degenerated problem. Other methods to observe Ganymede's atmosphere
582 are therefore highly needed to resolve this non-constrained issue.

583

584 **Acknowledgement:** F.L., R.M. and J.-Y.C. acknowledge the support by ANR of the TEMPETE project
585 (grant ANR-17-CE31-0016). Authors are also indebted to the "Système Solaire" and "Soleil
586 Héliosphère et Magnétosphère" programs of the French Space Agency CNES for their supports. Work
587 at Imperial College London was supported by the STFC of the UK under grant ST/W001071/1.
588 Authors also acknowledge the support of the IPSL data center CICLAD for providing us access to their
589 computing resources and data. Data may be obtained upon request from F. Leblanc
590 (email:francois.leblanc@latmos.ipsl.fr).

591

592

593 **References**

594 Ajello J.M., Kanik I., Ahmed S.M. and J.T. Clarke, Line profile of H Lyman α from dissociative excitation
595 of H₂ with application to Jupiter, *J. Geophys. Res.* et al., 100, E12, 26411-26420, 1995

596 Alday J., L. Roth, N. Ivchenko, K. D. Retherford, T. M. Becker, P. Molyneux, and J. Saur. New constraints
597 on Ganymede's hydrogen corona: Analysis of Lyman- α emissions observed by HST/STIS between 1998
598 and 2014. *Planet. Space Sci.*, 148:35-44, Nov 2017. doi: 10.1016/j.pss.2017.10.006.

599 Barth, C.A., Hord, C.W., Stewart, A.I.F., Pryor, W.R., Simmons, K.E., McClintock, W.E., Ajello, J.M.,
600 Naviaux, K.L. and Aiello, J.J.: Galileo ultraviolet spectrometer observations of atomic hydrogen in the
601 atmosphere of Ganymede, *Geophys. Res. Lett.*, 24, 2147–2150, 1997

602 Broadfoot A. L., Belton M. J., Takacs P. Z., Sandel B. R., Shemansky D. E., Holberg J. B., Ajello J. M., Moos
603 H. W., Atreya S. K., Donahue T. M., Bertaux J. L., Blamont J. E., Strobel D. F., McConnell J. C., Goody R.,
604 Dalgarno A., and McElroy M. B. Extreme ultraviolet observations from Voyager 1 encounter with
605 Jupiter. *Science*, 204:979–982, June 1979. doi: 10.1126/science.204.4396.979. URL
606 <http://adsabs.harvard.edu/abs/1979Sci...204..979B>.

607 Buccino D.R., Parisi M., Gramigna E., Gomez-Casajus L., Tortora P., Zannoni M., Caruso A., Park R.S.,
608 Withers P., Steffess P., Hodges A., Levin S. and Bolton S., Ganymede's Ionosphere observed by a Dual-
609 Frequency Radio Occultation with Juno, *Geophys. Res. Let*, 2022. doi: 10.1029/2022GL098420.

610 Carnielli G., Galand M. Leblanc F., L. Leclercq, Modolo R. and A. Beth, First 3D test particle
611 model of Ganymede's ionosphere, *Icarus*, 330, 42, 2019. <10.1016/j.icarus.2019.04.016> - insu-
612 02111422

613 Carnielli G., M. Galand, F. Leblanc, R. Modolo, A. Beth, X. Jia, Constraining Ganymede's neutral and
614 plasma environments through simulations of its ionosphere and Galileo observations, *Icarus*, 343,
615 113691, 2020a. <10.1016/j.icarus.2020.113691>

616 Carnielli G., M. Galand, F. Leblanc, R. Modolo, A. Beth, X. Jia, Simulations of ion sputtering at
617 Ganymede, *Icarus*, *Icarus*, 351, 113918, 2020b. <10.1016/j.icarus.2020.113918>

618 Cassidy T.A., C.P. Paranicas, J.H. Shirley, J.B. Dalton III, B.D. Teolis, R.E. Johnson, L. Kamp, A.R. Hendrix,
619 Magnetospheric ion sputtering and water ice grain size at Europa. *Planet. Space Sci.* **77**, 64–73 (2013).
620 <https://doi.org/10.1016/j.pss.2012.07.008>

621 Cooper J.F., R. E. Johnson, B. H. Mauk, H. B. Garrett, and N. Gehrels. Energetic Ion and Electron
622 Irradiation of the Icy Galilean Satellites. *Icarus*, 149(1):133-159, 2001. doi: 10.1006/icar.2000.6498.

623 Dalgarno A., Yan M., W. Liu, Electron energy deposition in a gas mixture of atomic and molecular
624 hydrogen and helium, *ApJS*, 125:237-256, 1999. 10.1086/313267

625 de Kleer K., Milby Z., Schmidt C., Camarca M. and M. Brown, The Optical Aurorae of Europa, Ganymede
626 and Callisto, *The Planetary Science Journal*, 4:37, 2023. <https://doi.org/10.3847/PSJ/acb53c>

627 Feldman, P.D., McGrath, M.A., Strobel, D.F., Warren Moos, H., Retherford, K.D., Wolven, B.C., HST/STIS
628 ultraviolet imaging of polar aurora on Ganymede. *Astrophys. J.* 535, 1085–1090, 2000.

629 Fray, N., Schmitt, B., Sublimation of ices of astrophysical interest: A bibliographic review. *Planet. Space*
630 *Sci.* 57, 2053–2080, <http://dx.doi.org/10.1016/j.pss.2009.09.011>, 2009.

631 Hall, D.T., Feldman, P.D., McGrath, M.A., Strobel, D.F., The far-ultraviolet oxygen airglow of Europa and
632 Ganymede, *The Astrophysical Journal* 499, 475, 1998.

633 Jia, X., Walker, R.J., Kivelson, M.G., Khurana, K.K., Linker, J.A., 2009. Properties of Ganymede's
634 magnetosphere inferred from improved three-dimensional MHD simulations. *Journal of Geophysical*
635 *Research (Space Physics)* 114, A09209. URL: <http://adsabs.harvard.edu/abs/2009JGRA..114.9209J>,
636 doi:<https://doi.org/10.1029/2009JA014375>.

637 Johnson P.V., J.W. McConkey, S.S. Tayal, and I. Kanik, Collisions of electrons with atomic oxygen:
638 current status, *Can. J. Phys.* 83: 589–616, 2005, doi: 10.1139/P05-034

639 Johnson, R.E., Carlson, R.W., Cooper, J.F., Paranicas, C., Moore, M.H., Wong, M.C., 2004. In: Bagenal,
640 F., Dowling, T., McKinnon, W. (Eds.), Jupiter Atmosphere, Satellites and Magnetosphere. Cambridge
641 Univ. Press, Cambridge, UK, pp. 485–512.

642 Johnson, R.E., A.V. Oza, F. Leblanc, C. Schmidt, T.A. Nordheim, The Origin and Fate of O₂ in Europa's
643 Ice: an Atmospheric Perspective, *Space Science Review*, 215, 1, 2019. <10.1007/s11214-019-0582-1> -
644 [insu-02020077](#)

645 Kanik I., C. Noren, 489 O. P. Makarov, P. Vatti Palle, J. M. Ajello, and D. E. Shemansky. Electron impact
646 dissociative excitation of O₂: 2. Absolute emission cross sections of the OI(130.4 nm) and OI(135.6 nm)
647 lines. *J. Geophys. Res.*, 108:5126, 2003.

648 Leblanc F., Leclercq L., A. Oza, C. Schmidt, Modolo R., J.Y. Chaufray and R.E. Johnson, On the orbital
649 variability of Ganymede's atmosphere *Icarus*, 293, 185-198, doi: 10.1016/j.icarus.2017.04.025, 2017.

650 Makarov, O. P., J. M. Ajello, P. Vattipalle, I. Kanik, M. C. Festou, and A. Bhardwaj, Kinetic energy
651 distributions and line profile measurements of dissociation products of water upon electron impact, *J.*
652 *Geophys. Res.*, 109, A09303, doi:10.1029/2002JA009353, 2004

653 Marconi, M.L., A kinetic model of Ganymede's atmosphere. *Icarus* 190, 155– 174, 2007.

654 Marzok, A., Schlegel, S., Saur, J., Roth, L., Grodent, D., Strobel, D. F., & Retherford, K. D. (2022).
655 Mapping the brightness of Ganymede's ultraviolet aurora using Hubble Space Telescope observations.
656 *Journal of Geophysical Research: Planets*, 127, e2022JE007256.
657 <https://doi.org/10.1029/2022JE007256>

658 McClintock W. E., G. J. Rottman, and T. N. Woods. Solar-Stellar Irradiance Comparison Experiment II
659 (Solstice II): Instrument Concept and Design. *Sol. Phys.*, 230:225-258, 2005.

660 McGrath, M.A., Xianzhe, J., Retherford, K., Feldman, P.D., Stroberl, D.F., Saur, J., Aurora on Ganymede.
661 *J. Geophys. Res.: Space Phys.* 118 (5), 2043–2054, 2013.

662 Modolo R., S. Hess, M. Mancini, F. Leblanc, JY Chaufray, D. Brain, L. Leclercq, G. Chanteur, P. Weill,
663 Gonzalez-Galindo, F. Forget, M. Yagi and C. Mazelle, Mars-solar wind interaction: LatHyS, an improved
664 parallel 3D multi-species hybrid model, *J. Geophys. Res.*, 121 (7), 6378-6399, 2016.

665 Molyneux P. M., J. D. Nichols, N. P. Bannister, E. J. Bunce, J. T. Clarke, S. W. H. Cowley, J. C. Gérard, D.
666 Grodent, S. E. Milan, and C. Paty. Hubble Space Telescope Observations of Variations in Ganymede's
667 Oxygen Atmosphere and Aurora. *Journal of Geophysical Research (Space Physics)*, 123(5):3777-3793,
668 2018. doi: 10.1029/2018JA025243.

669 Musacchio, F., J. Saur, L. Roth, K. D. Retherford, M. A. McGrath, P. D. Feldman, and D. F. Strobel (2017),
670 Morphology of Ganymede's FUV auroral ovals, *J. Geophys. Res. Space Physics*, 122, 2855–2876,
671 doi:10.1002/2016JA023220.

672 Neubauer, F.M., The sub-Alfvénic interaction of the Galilean satellites with the Jovian magnetosphere.
673 *Journal of Geophysical Research* 104 (E2), 3863, 1999. <http://doi.wiley.com/10.1029/1998JE900031>

674 Oren M. and Nayar S. K., Generalization of Lambert's Reflectance Model, *Proceedings of the 21st*
675 *Annual Conference on Computer Graphics and Interactive Techniques*: 239–246, 1994.
676 [doi:10.1145/192161.192213](https://doi.org/10.1145/192161.192213)

677 Oza A. V., F. Leblanc, R. E. Johnson, C. Schmidt, L. Leclercq, Cassidy T. and J.Y. Chaufray, Dusk over dawn
678 O₂ asymmetry in Europa's near-surface atmosphere, *Planetary & Space Science*, 167, 23-32, 2019.
679 doi.org/10.1016/j.pss.2019.01.006

680 Plainaki, C., Milillo, A. , Massetti, S. , Mura, A., Jia, X., Orsini, S., Mangano, V., DeAngelis, E., Rispoli, R.,
681 The H₂O and O₂ exospheres of Ganymede: the result of a complex interaction between the jovian
682 magnetospheric ions and the icy moon, *Icarus*, 245, 306–319,
683 <http://dx.doi.org/10.1016/j.icarus.2014.09.018>, 2015.

684 Plainaki C., G. Sindoni, D. Grassi, L. Cafarelli, E. D'Aversa, S. Massetti, A. Mura, A. Milillo, G. Filacchione,
685 G. Piccioni, Y. Langevin, F. Poulet, F. Tosi, A. Migliorini, and F. Altieri. Preliminary estimation of the

686 detection possibilities of Ganymede's water vapor environment with MAJIS. *Planet. Space Sci.*,
687 191:105004, 2020a, doi: 10.1016/j.pss.2020.105004.

688 Plainaki C., S. Massetti, X. Jia, A. Mura, A. Milillo, D. Grassi, G. Sindoni, E. D'Aversa, and G. Filacchione.
689 Kinetic Simulations of the Jovian Energetic Ion Circulation around Ganymede. *ApJ*, 900(1):74, 2020a.
690 doi: 10.3847/1538-4357/aba94c.

691 Roth L., J. Saur, K. D. Retherford, P. D. Feldman, and D. F. Strobel. A phenomenological model of Io's
692 UV aurora based on HST/STIS observations. *Icarus*, 228:386-406, 2014.

693 Roth L., J. Saur, K. D. Retherford, D. F. Strobel, P. D. Feldman, M. A. McGrath, J. R. Spencer, A. Blöcker,
694 and N. Ivchenko. Europa's far ultraviolet oxygen aurora from a comprehensive set of HST observations.
695 *Journal of Geophysical Research (Space Physics)*, 121:2143-2170, March 2016.

696 Roth L. et al., Evidence for a sublimated water atmosphere on Ganymede from Hubble Space Telescope
697 Observations, *Nature*, 2021

698 Roth L., C. Plainaki, A.V. Oza, A. Vorburger, R.E. Johnson, P.M. Moyneux, K.D. Retherford, F. Leblanc, S.
699 Massetti, A. Mura and P. Wurz, Ganymede's tenuous atmosphere, *Ganymede book*, 2022

700 Roth L., Marchesini G., Becker T.M., Hoeijmakers H.J., Molyneux, P.M., Retherford K.D., Saur J.,
701 Carberry Mogan S.R. and J.R. Szalay, Probing Ganymede's Atmosphere with HST Ly α Images in Transit
702 of Jupiter, *The Planetary Science Journal*, 4:12, 2023. <https://doi.org/10.3847/PSJ/acaf7f>

703 Saur, J., Duling, S., Roth, L., Jia, X., Strobel, D. F., Feldman, P. D., et al. (2015). The search for a subsurface
704 ocean in Ganymede with Hubble Space Telescope observations of its auroral ovals. *Journal of*
705 *Geophysical Research: Space Physics*, 120(3), 1715–1737. <https://doi.org/10.1002/2014JA020778>

706 Shemansky D.E., Yung Y.L., Liu W., Yoshii J., Hansen C.J., Hendrix A.R. and L.W. Esposito, A new
707 understanding of the Europa Atmosphere and limits on geophysical activity, *ApJ*, 797-84, 2014. doi:
708 10.1088/0004-637X/797/2/84

709 Shematovich, V.I., Neutral Atmosphere Near the Icy Surface of Jupiter's Moon Ganymede, Solar System
710 Research, 2016, 50, 4, 262–280, 2016.

711 Song M.Y., Hyuck C., Karwasz G.P., Kokoouline V., Nakamura Y., Tennyson J., Faure A., Mason N.J. and
712 Y. Itikawa, J. Phys. Chem. Ref. Data 50, 023103 (2021). doi: 10.1063/5.0035315

713 Spencer, J.R., Icy Galilean satellite reflectance spectra: less ice on Ganymede and Callisto? Icarus 70,
714 99–110, 1987.

715 Spencer J. R., L. A. Lebofsky, and M. V. Sykes. Systematic biases in radiometric diameter
716 determinations. Icarus, 78(2):337{354, 1989. doi: 10.1016/0019-1035(89)90182-6.

717 Stern, S.A., The lunar atmosphere: history, status, current problems and context, Reviews of
718 Geophysics, 37, 4, 453–491, 1999.

719 Tayal S.S. and O. Zatsarinny, *B-spline R-matrix-with-pseudostates* approach for excitation and
720 ionization of atomic oxygen by electron collisions, Physical Review A 94, 042707, 2016. doi:
721 10.1103/PhysRevA.94.042707

722 Turc, L., Leclercq, L., Leblanc, F., Modolo, R., Chaufray, J.-Y., Modelling Ganymede's neutral
723 environment: A 3D test-particle simulation. Icarus 229, 157–169, 2014.

724 Vasyliūnas V.M. and A. Eviatar, Outflow of ions from Ganymede: a reinterpretation, Geophys. Res. Let.,
725 27, 9, 1347-1349, 2000.

726 Vorburgeter A., Fatemi S., Galli A., Liuzzo L., Poppe A.R. and P. Wurz, 3D Monte-Carlo simulation of
727 Ganymede's water exosphere, Icarus, 375, 114810, 2022.
728 <https://doi.org/10.1016/j.icarus.2021.114810>